Data-Driven and Robust Path-following Control of a Quadrotor Slung Load Transport System

Hei Shing Helson Go*, Longhao Qian† and Hugh H.T. Liu ‡.
University of Toronto Institute for Aerospace Studies, 4925 Dufferin St, North York, Canada, ON M3H 5T6

In this paper, a robust path following control law for a quadrotor Slung Load Transport System is developed. A Gaussian Process-augmented Extended Kalman Filter is proposed to estimate payload states. In this approach, Gaussian Processes are used to compensate for unmodelled dynamics in the process model, and they are trained on previously collected data of a Slung Load Transport System in flight. Both simulations and experiments verify the estimation and control system framework and demonstrate successful stabilization and trajectory tracking of the Slung Load Transport System, overcoming model inaccuracy and disturbances.

I. Nomenclature

$\underrightarrow{\mathcal{F}}_i$	=	NED inertial frame
$\underrightarrow{\mathcal{F}}_b$	=	Quadrotor body-fixed frame, fixed at the mass center of the quadrotor vehicle
m_b	=	Quadrotor mass
$\mathbf{J}_b$	=	Quadrotor moment of inertia
m_p	=	Payload mass
l	=	Cable length
$\mathbf{g}_I$	=	Gravity vector in the world frame
$\boldsymbol{\ell} \in \mathbb{R}^3$	=	Vector spanning the length of the cable
$\mathbf{x}_p \in \mathbb{R}^3$	=	Absolute position of the payload mass center
$\mathbf{v}_p \in \mathbb{R}^3$	=	Absolute velocity of the payload mass center, expressed in $\underrightarrow{\mathcal{F}}_i$
$\mathbf{r} \in \mathbb{R}^2$	=	Relative position of the quadrotor mass center w.r.t. the payload, projected onto the XY plane of $\underrightarrow{\mathcal{F}}_i$
$\mathbf{v} \in \mathbb{R}^2$	=	Relative velocity of the quadrotor mass center w.r.t. the payload, projected onto the XY plane of $\underrightarrow{\mathcal{F}}_i$
$\tilde{\dot{\mathbf{v}}} \in \mathbb{R}^2$	=	Difference between $\dot{\mathbf{v}}$ predicted by some dynamics model and the true value
$\mathbf{B} \in \mathbb{R}^{3\times2}$	=	Projection from $\mathbf{v}$ to the time derivative of $\boldsymbol{\ell}$
$\mathbf{R}_{ib} \in \mathrm{SO}(3)$	=	Rotation of $\underrightarrow{\mathcal{F}}_i$ relative to $\underrightarrow{\mathcal{F}}_b$
$\boldsymbol{\omega}_b \in \mathbb{R}^3$	=	Angular velocity of the $\underrightarrow{\mathcal{F}}_b$ relative to $\underrightarrow{\mathcal{F}}_i$, expressed in $\underrightarrow{\mathcal{F}}_b$
$\mathbf{f}_L \in \mathbb{R}^3$	=	Total thrust delivered by the actuators
$\boldsymbol{\tau} \in \mathbb{R}^3$	=	Total torque delivered by the actuators
$\mathbf{d}_p \in \mathbb{R}^3$	=	Disturbance acting on the payload
$\mathbf{d}_b \in \mathbb{R}^3$	=	Disturbance acting on the quadrotor body
$\mathbf{d}_T \in \mathbb{R}^3$	=	Sum of disturbances acting on the SLTS
$\mathbf{e}_p \in \mathbb{R}^3$	=	Positional (radial) error of the payload from some given path
$\mathbf{e}_v \in \mathbb{R}^3$	=	Velocity (tangential) error of the payload from some given path
$\times : \mathbb{R}^3 \to \mathbb{R}^{3\times3}$	=	Maps a 3-vector to a 3-by-3 skew-symmetric (*cross product*) matrix
$\vee : \mathbb{R}^{3\times3} \to \mathbb{R}^3$	=	The inverse operation of the $\times$ mapping

*Ph.D. Candidate, hei.go@mail.utoronto.ca
†Ph.D., longhao.qian@mail.utoronto.ca.
‡Professor, hugh.liu@utoronto.ca; AIAA Associate Fellow

II. Introduction

Drone delivery is an emerging application of Unmanned Aerial Vehicles. Slung Load Transport Systems (SLTS), i.e. carrying a slung payload externally with a cable, is one approach proposed for payload delivery. Extensive studies have been done on developing payload stabilization and trajectory tracking [1–4] for SLTS. Various methodologies such as geometric control [2], adaptive control [3], and passivity-based control [4] have been proposed or adopted. Successful development of dynamics models for SLTS [2, 5] also ushered in an abundance of works applying Optimal Controllers or Model Predictive Controllers (MPC) [6, 7] to SLTS control. In our own previous work, a dynamics model for SLTS [8] was developed and a robust path-following controller was designed based on the Active Disturbance Rejection Controller (ADRC) concept. This controller has been applied to control both simple SLTS with a single vehicle and payload [9], and *cooperative* SLTS where multiple quadrotor UAVs carry a single payload [10, 11], to carry out path following in the presence of disturbances. This controller is also proven to be exponentially stable [11] and requires no feedback of higher order motion terms, e.g. snap/jerk.

A key challenge in developing controllers for SLTS is implementing payload tracking and pose estimation to provide feedback, whereas many previous works carried out simulations only or relied on *instrumented* payloads. In the case of our own previous work, high-precision motion capture systems were used. Zurn *et. al.* [6] used an onboard camera to track a payload tagged by Aruco visual fiducial tags that enable direct payload pose sensing for an MPC. Tang *et. al.* [12] made use of a downward-facing camera to track a slung load, while measurements are filtered by an Extended Kalman Filter (EKF). Li [7] proposed an MPC framework where a tagged payload is tracked by a computer vision and an EKF is used to estimate payload pose. Despite their promise, Kalman Filters built on vision-based payload trackers employ SLTS dynamics models as their process models, so their performance is readily impacted by model uncertainty or mismatch.

However, compensating for model inaccuracy in SLTS dynamics remains an open question. A major focus of ongoing research is addressing uncertainty in payload inertial parameters [13–15]. Aghdam *et. al.* [13] modeled varying payload center-of-mass as a mass-spring system. Li *at. al.* used the parameter-robust Linear Quadratic Gaussian controller to achieve robustness against payload mass variation. Another aspect of model inaccuracy in SLTS dynamics is that the dynamics of the cable itself are often neglected, even though it is shown to be a significant component of SLTS dynamics. Goodarzi *et. al.* modeled an SLTS treating the cable as serially connected links [16] and designed a geometric controller to bring the SLTS to the desired position while minimizing cable flex [17, 18]. Kotaru *et. al.* showed that a geometric controller developed under the inelastic cable assumption remains viable after considering cable elasticity [19]. As for identifying and correcting for model uncertainty and disturbances in general, two works employing machine learning techniques [20, 21] have been identified to the best of our ability. Kang *et. al.* proposed a slung load controller in which a nonlinear payload oscillation damper is extended by an adaptive neural network to correct for model uncertainty or wind gusts [20]. Vargas and Enrique trained an unstructured black-box algorithm that estimates the load position given quadrotor pose and pilot inputs [21].

Data-driven estimation [22, 23] is identified as another potential answer to this question. This concept exploits Gaussian Processes (GP) [24], trained on empirical data, to estimate model uncertainty or mismatch, which can be applied as a correction to some nominal dynamics model. Ko and Fox proposed substituting GPs for process or observation models in various Bayesian filters, including the EKF [23]. They demonstrated that GP-augmented filters improve estimation accuracy that would otherwise be impaired by model mismatch.

In this paper, our main contribution is proposing a novel Gaussian Process-augmented Extended Kalman Filter to estimate payload states for a robust controller for SLTS, which is based on the framework in [11]. Our estimation and control framework is depicted in Figure 1.

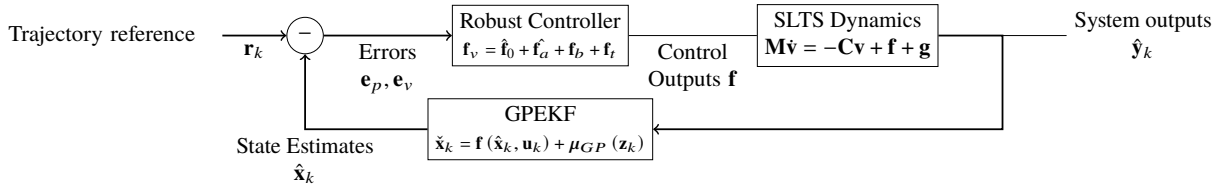

Fig. 1 Proposed system architecture

The remainder of this paper is organized as follows. In section III, the SLTS dynamics model and the robust path-following controller are reviewed. In sections IV, the Gaussian Process concept is introduced and in section V, the GP-EKF is outlined. Finally, in section VI, experimental results are presented.

III. Problem Formulation

A. SLTS Dynamics

Our nominal model of SLTS dynamics is taken from that in [10] and specialized for a single quadrotor. A quadrotor with mass m_b attached to a payload with mass m_p by a cable with length l is considered. The NED inertial frame is denoted by $\underset{\rightarrow}{\mathcal{F}}_i$ and the quadrotor body-fixed frame is denoted by $\underset{\rightarrow}{\mathcal{F}}_b$. The vector spanning the length of the cable is $\boldsymbol{\ell} \in \mathbb{R}^3$. Its projection on the x/y-plane of $\underset{\rightarrow}{\mathcal{F}}_i$ is $\mathbf{r} \coloneqq \boldsymbol{\ell}_{1:2}$. The SLTS is visualized in Fig. 2.

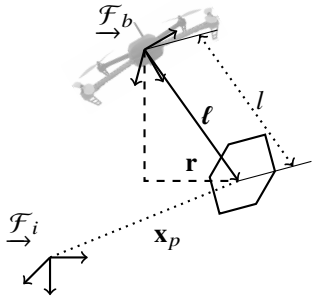

Fig. 2 SLTS geometry

Since the cable has a fixed length viz. $\|\boldsymbol{\ell}\| \equiv l$, the 2-vector $\mathbf{r}$ sufficiently describes the quadrotor's position relative to the payload. Similarly, the quadrotor's velocity relative to the payload is described by a 2-vector $\mathbf{v} \coloneqq \dot{\mathbf{r}}$. Together, $\{\mathbf{r}, \mathbf{v}\}$ fully define $\boldsymbol{\ell}$ and $\dot{\boldsymbol{\ell}}$, which embody the 3D position and velocity of the payload relative to the quadrotor UAV

$$\boldsymbol{\ell} = \begin{bmatrix} \mathbf{r} \\ -\sqrt{l^2 - \mathbf{r}^\top \mathbf{r}} \end{bmatrix} \quad \dot{\boldsymbol{\ell}} \coloneqq \underbrace{\begin{bmatrix} \mathbf{1}_{2\times 2} \\ \frac{\mathbf{r}^\top}{\sqrt{l^2 - \mathbf{r}^\top \mathbf{r}}} \end{bmatrix}}_{\mathbf{B}} \underbrace{\dot{\mathbf{r}}}_{\mathbf{v}} = \mathbf{B}\mathbf{v} \tag{1}$$

The equations of motion of the slung load transport system are defined below.

1. SLTS Rotational Dynamics

The states of the SLTS rotational subsystem are $\mathcal{X}_{\text{rot}} : \{\mathbf{R}_{ib}, \boldsymbol{\omega}_b\}$. The input to the SLTS rotational subsystem is the torque acting on the quadrotor body $\mathcal{U}_{\text{rot}} : \{\boldsymbol{\tau}\}$. Thus the SLTS rotational equations of motion are

$$\Sigma_{\text{rot}} : \begin{cases} \mathbf{J}\dot{\boldsymbol{\omega}}_b &= -\boldsymbol{\omega}_b^{\times}\mathbf{J}\boldsymbol{\omega}_b + \boldsymbol{\tau} \\ \dot{\mathbf{R}}_{ib} &= \mathbf{R}_{ib}\boldsymbol{\omega}_b^{\times} \end{cases} \tag{2}$$

2. SLTS translational dynamics

The states of the SLTS translational subsystem are $\mathcal{X}_{\text{trans}} : \{\mathbf{x}_p, \mathbf{r}, \mathbf{v}_p, \mathbf{v}\}$. These states are grouped into the generalized coordinate vector $\boldsymbol{x} = \begin{bmatrix} \mathbf{x}_p^\top & \mathbf{r}^\top \end{bmatrix}$ and the block velocity vector $\boldsymbol{u} = \begin{bmatrix} \mathbf{v}_p^\top & \mathbf{v}^\top \end{bmatrix}^\top$. The input to the SLTS translational subsystem is thrust acting on the quadrotor body $\mathcal{U}_{\text{trans}} = \{\mathbf{f}_L\}$, which is in practice treated as a scalar thrust aligned to the z-axis of $\underset{\rightarrow}{\mathcal{F}}_b$, so $\mathbf{f}_L = f_L \mathbf{R}_{ib}\mathbf{1}_3$. Hence, the SLTS translational equations of motion are

$$\Sigma_{\text{trans}} : \begin{cases} \dot{\boldsymbol{x}} &= \boldsymbol{u} \\ \dot{\boldsymbol{u}} &= \boldsymbol{M}^{-1}\left(-\boldsymbol{C}\boldsymbol{u} + \boldsymbol{f} + \boldsymbol{g}\right) \end{cases} \tag{3}$$

$$\text{where } \boldsymbol{M} = \begin{bmatrix} (m_p + m_b)\mathbf{1} & m_b\mathbf{B} \\ m_b\mathbf{B}^\top & m_b\mathbf{B}^\top\mathbf{B} \end{bmatrix} \quad \boldsymbol{C} = \begin{bmatrix} \mathbf{0} & m_b\dot{\mathbf{B}} \\ \mathbf{0} & m_b\mathbf{B}^\top\dot{\mathbf{B}} \end{bmatrix} \quad \boldsymbol{f} = \begin{bmatrix} \mathbf{f}_L \\ \mathbf{B}^\top\mathbf{f}_L \end{bmatrix} \quad \boldsymbol{g} = \boldsymbol{M}\begin{bmatrix} \mathbf{g}_I \\ \mathbf{0} \end{bmatrix} \tag{4}$$

An alternative notation for (3), when it is used individually as a state equation in estimator design, is $\dot{\mathbf{x}} = \mathbf{f}(\mathbf{x}, \mathbf{u})$, where $\mathbf{x} \in \mathbb{R}^{10}$ and $\mathbf{u} \in \mathbb{R}^3$ are the state and input vectors formed by stacking elements in $\mathcal{X}_{\text{trans}}$ and $\mathcal{U}_{\text{trans}}$ respectively.

B. Robust Path-Following Controller

A robust controller for the SLTS is designed based on that proposed in [11] and specialized for a single quadrotor UAV.

Firstly, the control law corrects for a position error $\mathbf{e}_p \in \mathbb{R}^3$ and a velocity error $\mathbf{e}_v \in \mathbb{R}^3$ of the payload. Given an initial waypoint $\mathbf{p}^j$ and a destination waypoint $\mathbf{p}^{j+1}$ for the payload, the position error is simply the perpendicular distance between the payload position $\mathbf{x}_p$ and the line between the two waypoints,

$$\mathbf{e}_p = \mathbf{x}_p - \mathbf{p}^j - \left(\mathbf{x}_p - \mathbf{p}^j\right)^\top \mathbf{n}_j^{j+1} \mathbf{n}_j^{j+1} \tag{5}$$

where $\mathbf{n}_j^{j+1}$ is the unit heading vector between the waypoints and $\mathbf{v}_d$. Next, the velocity error is

$$\mathbf{e}_v = \mathbf{v}_p - \mathbf{v}_d \tag{6}$$

where $\mathbf{v}_d$ is the desired velocity vector defined by some cruise speed $v_{\text{cruise}} \in \mathbb{R}^+$ multiplied to $\mathbf{n}_j^{j+1}$.

Secondly, the control law minimizes payload displacement at *equilibrium*, embodied by the payload swing error $\hat{\boldsymbol{\mu}}$

$$\hat{\boldsymbol{\mu}} = k_L \left(\mathbf{r} - \hat{\mathbf{r}}_d\right) \quad \text{where } \hat{\mathbf{r}}_d = l \frac{\hat{\mathbf{d}}_{T\,1:2}}{\left\| m_g \mathbf{g}_I - \hat{\mathbf{d}}_T \right\|} \tag{7}$$

where $\hat{\mathbf{r}}_d$ is the equilibrium payload position, dependent on the disturbance acting on the SLTS $\hat{\mathbf{d}}_T$, itself estimated by

$$\hat{\mathbf{d}}_T \coloneqq \lambda_T \left((m_p + m_b)\mathbf{v}_p + m_b \mathbf{B}\mathbf{v} - \int_0^t (\mathbf{f}_L + \hat{\mathbf{d}}_\perp) + \hat{\mathbf{d}}_T + (m_p + m_b)\mathbf{g}_I \, d\tau \right) \tag{8}$$

$$\text{where } \hat{\mathbf{d}}_b \coloneqq \kappa \int_0^t \mathfrak{B}(\mathbf{d}_b - \hat{\mathbf{d}}_b) d\tau \quad \hat{\mathbf{d}}_\perp \coloneqq \left(\mathbf{1} - \frac{\boldsymbol{\ell}\boldsymbol{\ell}^\top}{l^2} \right) \hat{\mathbf{d}}_b \quad \mathfrak{B} = \mathbf{B} \left(\mathbf{B}^\top \mathbf{B} \right)^{-1} \mathbf{B}^\top \tag{9}$$

Hence, the control law is given by

$$\mathbf{f}_v = \hat{\mathbf{f}}_0 + \hat{\mathbf{f}}_a + \mathbf{f}_b + \mathbf{f}_t \quad \text{where} \begin{array}{ll} \hat{\mathbf{f}}_0 = -m_b \left(\dot{\hat{\boldsymbol{\zeta}}} + k_L \mathbf{B}\mathbf{v} + \dot{\mathbf{B}}\hat{\boldsymbol{\mu}} \right) & \hat{\boldsymbol{\zeta}} = k_p \mathbf{e}_p + \hat{\mathrm{F}} - \mathbf{v}_d \\ \hat{\mathbf{f}}_a = -K_0 \left(\mathbf{v}_p + \hat{\boldsymbol{\zeta}} + \mathbf{B}\left(\mathbf{v} + \hat{\boldsymbol{\mu}}\right) \right) & \hat{\mathrm{F}} = \displaystyle\int_0^t -\lambda \hat{\mathrm{F}}(\tau) + k_r \hat{\mathrm{R}}(\tau) d\tau \\ \mathbf{f}_b = m_b \left(\dot{\boldsymbol{\zeta}} + k_p \mathbf{s}_p \right) & \hat{\mathrm{R}} = \mathbf{B}\left(\mathbf{v} + \hat{\boldsymbol{\mu}}\right) \\ \mathbf{f}_t = -m_b \mathbf{g} + \hat{\mathbf{f}}_d - \hat{\mathbf{d}}_\perp & \hat{\mathbf{f}}_d = -(m_p \mathbf{g}_I + \hat{\mathbf{d}}_T) \end{array} \tag{10}$$

The exponential stability of this controller can be proven by specializing the procedure in [11], taking the number of vehicles to be 1 and ignoring all terms about multi-quadrotor collaboration.

C. Attitude Tracking Controller

The attitude tracking controller serves the above path-following controller by sending a torque input $\boldsymbol{\tau}$ to the rotational subsystem Σ_{rot} and a thrust input f_L to the translational subsystem Σ_{trans} to deliver $\mathbf{f}_v$. The thrust input is obtained directly as $f_L = \|\mathbf{f}_v\|$. The torque input $\boldsymbol{\tau}$ is computed from a desired attitude $\mathbf{R}_{ib_d} \in SO(3)$ given by

$$\mathbf{R}_{ib_d} = \begin{bmatrix} \mathbf{n}_x & \mathbf{n}_y & \mathbf{n}_z \end{bmatrix} \text{ where } \mathbf{n}_z = \frac{\mathbf{f}_v}{f_L} \quad \mathbf{n}_x = \begin{bmatrix} \cos\psi_d & \sin\psi_d & -\frac{\cos\psi_d \mathbf{n}_{z1} + \sin\psi_d \mathbf{n}_{z2}}{\mathbf{n}_{z3}} \end{bmatrix}^\top \quad \mathbf{n}_y = \frac{\mathbf{n}_z^\times \mathbf{n}_x}{\left\| \mathbf{n}_z^\times \mathbf{n}_x \right\|} \tag{11}$$

where the desired heading angle $\psi_d \in [-\pi, \pi)$ is arbitrarily specified.

The desired attitude $\mathbf{R}_{ib_d}$ and desired angular velocity $\boldsymbol{\omega}_{b_d}$ is set of states $\left\{\mathbf{R}_{ib_d}, \boldsymbol{\omega}_{b_d}\right\}$ to be tracked. Any controller capable of driving some suitably defined rotation errors $\tilde{\mathcal{X}}_{\text{rot}} = \left\{\tilde{\mathbf{R}}, \tilde{\boldsymbol{\omega}}\right\}$ to zero can preserve the upstream robust path-following controller's stability properties. Roza and Maggiore [25]'s Almost Globally Asymptotically Stable (AGAS) attitude tracker is viable for this purpose. Here, the desired angular velocity is determined by $\boldsymbol{\omega}_d = \left(\mathbf{R}_{ib_d}^\top \dot{\mathbf{R}}_{ib_d} \right)^\vee$, the attitude error is $\tilde{\mathbf{R}} = \mathbf{R}_{ib_d}^\top \mathbf{R}_{ib}$, the angular velocity error is $\tilde{\boldsymbol{\omega}} = \boldsymbol{\omega}_b - \mathbf{R}^\top \boldsymbol{\omega}_{b_d}$, and the control law is

$$\boldsymbol{\tau} = -b_\omega \tilde{\boldsymbol{\omega}}_b - b_r \boldsymbol{e}_r - \tilde{\boldsymbol{\omega}}_b^\times \boldsymbol{J} \tilde{\boldsymbol{\omega}}_b + \boldsymbol{\omega}_b^\times \boldsymbol{J} \boldsymbol{\omega} - \boldsymbol{J} \left(\tilde{\boldsymbol{\omega}}_b^\times \tilde{\mathbf{R}}^\top \boldsymbol{\omega}_d - \tilde{\mathbf{R}}^\top \dot{\boldsymbol{\omega}}_d \right) \quad \text{where } \boldsymbol{e}_r = \sum_{i=1}^{3} \boldsymbol{e}_i^\times \tilde{\mathbf{R}} \boldsymbol{e}_i. \tag{12}$$

IV. Gaussian Process-Approximated SLTS dynamics

Gaussian Processes (GP) [22, 24] are used to predict errors in the SLTS dynamics and compensate for them. The unobservable true SLTS dynamics are denoted by $\mathbf{f}_{\text{true}}$, which is measured by $\hat{\mathbf{y}}$

$$\hat{\mathbf{y}} = \mathbf{f}_{\text{true}}(\mathbf{x}, \mathbf{u}) + \mathbf{w} \tag{13}$$

where disturbances, noise and model errors are embodied in $\mathbf{w} \sim \mathcal{N}(\mathbf{0}, \boldsymbol{\Sigma})$, assumed to be Gaussian.

The corrected SLTS dynamics is denoted by $\mathbf{f}^*$ and composed of the nominal SLTS model $\mathbf{f}$, which implements the dynamical equation in equation (3), plus the GP correction

$$\mathbf{f}^*(\mathbf{x}, \mathbf{u}) = \underbrace{\mathbf{f}(\mathbf{x}, \mathbf{u})}_{\boldsymbol{M}^{-1}(-\boldsymbol{C}\boldsymbol{u}+\boldsymbol{f}+\boldsymbol{g})} + \mathbf{B}_d \boldsymbol{\mu}(\mathbf{z}) \tag{14}$$

where $\boldsymbol{\mu}$ is the *a-posteriori* mean of the GP, $\mathbf{z}$ is the Gaussian Process input formed from a subset of $\{\mathbf{x}, \mathbf{u}\}$, and $\mathbf{B}_d$ is a projection from the output space of the GP to the state space of the dynamical equation. Furthermore, the training feature samples are denoted by $\mathbf{Z}$ and the test point by $\mathbf{z}_*$. As such, the posterior distribution at $\mathbf{z}_*$ is also Gaussian with mean and covariance

$$\begin{aligned} \boldsymbol{\mu}(\mathbf{z}_*) &= \mathbf{k}_*^\top \left(\mathbf{K} + \sigma_n^2 \mathbf{1}\right)^{-1} \mathbf{z} \\ \boldsymbol{\Sigma}(\mathbf{z}_*) &= \kappa(\mathbf{z}_*, \mathbf{z}_*) - \mathbf{k}_*^\top \left(\mathbf{K} + \sigma_n^2 \mathbf{1}\right)^{-1} \mathbf{k}_* \end{aligned} \quad \text{where} \quad \begin{aligned} \mathbf{k}_* &= \kappa(\mathbf{z}_*, \mathbf{Z}) \\ \mathbf{K} &= \kappa(\mathbf{Z}, \mathbf{Z}) + \sigma_n^2 \mathbf{1} \end{aligned} \tag{15}$$

where the kernel function κ is chosen to be the Squared Exponential Kernel. Its definition is given by

$$\kappa(\mathbf{z}_i, \mathbf{z}_j) \coloneqq \sigma_f^2 \exp\left(-\frac{1}{2}(\mathbf{z}_i - \mathbf{z}_j)^\top \mathbf{W}^{-1}(\mathbf{z}_i - \mathbf{z}_j)\right) + \sigma_n^2 \tag{16}$$

where $\mathbf{W} \triangleq \text{diag}(\boldsymbol{\ell}^2)$ is a diagonal matrix of length scales, σ_f^2 is the process variance, and σ_n^2 the noise variance.

In our formulation, the true payload acceleration relative to the quadrotor UAV is assumed to contain a component that embodies the error between actual system dynamics and the nominal model. Physically, this component is considered to encompass effects of variation of payload mass, aerodynamic effects and drag on the payload, dynamics of cable elasticity or flex, etc. This quantity is named the payload acceleration error $\tilde{\dot{\mathbf{v}}}$ and is assumed to be a function of payload relative position $\mathbf{r}$ and velocity $\mathbf{v}$. The GP acts as this function and estimates $\tilde{\dot{\mathbf{v}}}$. In the notation of (14), this is written as

$$\tilde{\dot{\mathbf{v}}} = \boldsymbol{\mu}(\mathbf{z}) \quad \text{where } \mathbf{z} \coloneqq \begin{bmatrix} \mathbf{r} \\ \mathbf{v} \end{bmatrix} \tag{17}$$

The hyperparameters $(\boldsymbol{\ell}, \sigma_f, \sigma_n)$ in the kernel function (16) determine the behavior of $\boldsymbol{\mu}$ and thereby the quantitative mapping from $(\mathbf{r}, \mathbf{v})$ to $\tilde{\dot{\mathbf{v}}}$. To determine these hyperparameters (c.f. *fitting* the GP), maximum likelihood optimization is performed on previously collected data. In creating this dataset, for each sample k the payload acceleration errors are computed by

$$\tilde{\dot{\mathbf{v}}}_k = \frac{\mathbf{v}_{k+1} - \hat{\mathbf{v}}_{k+1}}{\delta T_k} \tag{18}$$

where the predicted payload velocity $\hat{\mathbf{v}}_{k+1}$ is given by the base dynamical equation (3) and the actual payload velocity at the next timestep $\mathbf{v}_{k+1}$ is measured.

V. Payload State Estimation

The purpose of state estimation is to employ our SLTS dynamics model and sensor measurements to methodically estimate states in the SLTS with the aid of potentially intermittent or noisy exteroceptive measurements.

A. State Dynamics

The estimator states are the states of the SLTS translational subsystem $\mathbf{x} \triangleq \begin{bmatrix}\mathbf{x}_p^\top & \mathbf{r}^\top & \mathbf{v}_p^\top & \mathbf{v}^\top\end{bmatrix}$, and the estimator inputs are identical to that of the SLTS translational subsystem $\mathbf{u} = \mathbf{f}_L$. The state dynamics equations are the SLTS translational equations of motion *augmented by GP correction*.

$$\mathbf{f}(\mathbf{x}, \mathbf{u}) : \begin{cases} \dot{\boldsymbol{x}} &= \boldsymbol{u} \\ \dot{\boldsymbol{u}} &= \boldsymbol{M}\left(-\boldsymbol{C}\boldsymbol{u} + \boldsymbol{f} + \boldsymbol{g}\right) + \mathbf{B}_d \boldsymbol{\mu}(z) \end{cases} \tag{19}$$

The discrete state dynamics are obtained by integrating equation (19) by the Euler method. The nominal dynamics portion of the state dynamics equation is linearized by a symbolic algebra application, while the GP prediction is differentiated using the means outlined in [26].

$$\frac{\partial \boldsymbol{\mu}(\mathbf{z})}{\partial \mathbf{x}} = \frac{\partial \mathbf{k}^*}{\partial \mathbf{z}} \left(\left(\mathbf{K} + \sigma_n^2 \mathbf{1} \right)^{-1} \mathbf{z} \right) \frac{\partial \mathbf{z}}{\partial \mathbf{x}} \tag{20}$$

where $\mathbf{z}$ is defined in equation (17), so the final partial derivative is a simple projection from the state $\mathbf{x}$ to the selected GP features $(\mathbf{r}, \mathbf{v})$.

The linearized system and input matrices are denoted by $\mathbf{F}_k$ and $\mathbf{G}_k$. The inputs $\mathbf{f}_L$ are affected by noise, assumed to be drawn from a zero-mean multivariate Gaussian distribution, for a diagonal covariance matrix $\mathbf{Q} \in \mathbb{R}^{3\times3}$

B. Measurement Model

The measurement model describes the relationship between the system states and exteroceptive measurements. Three sources of exteroceptive measurements are considered

1) Quadrotor absolute position, output by GNSS/INS positioning modules
2) Quadrotor absolute velocity, output by GNSS/INS positioning modules
3) Payload position relative to the quadrotor, likely measured by a vision-based method

which are modeled by the following equations

$$\mathbf{h}(\mathbf{x}_k) = \begin{bmatrix} \mathbf{h}_{\text{abs-pos}}(\mathbf{x}_k) \\ \mathbf{h}_{\text{abs-vel}}(\mathbf{x}_k) \\ \mathbf{h}_{\text{rel}}(\mathbf{x}_k) \end{bmatrix} \quad \begin{aligned} \mathbf{h}_{\text{abs-pos}}(\mathbf{x}_k) &= \mathbf{x}_p + \boldsymbol{\ell} \\ \text{where } \mathbf{h}_{\text{abs-vel}}(\mathbf{x}_k) &= \mathbf{v}_p + \mathbf{B}\mathbf{v} \\ \mathbf{h}_{\text{rel}}(\mathbf{x}_k) &= \boldsymbol{\ell} \end{aligned} \tag{21}$$

These equations are also linearized by a symbolic algebra application and the linearized measurement matrix is denoted by $\mathbf{H}_k$. Similarly, the measurements are assumed to be affected by zero-mean Gaussian noise, making for a diagonal covariance matrix $\mathbf{R} \in \mathbb{R}^{9\times9}$

C. Extended Kalman Filter

Payload state estimation is implemented as a standard Extended Kalman Filter

1) *Prediction*: In the prediction step, a new state estimate and error covariance estimate are computed using the state dynamics model (19) and the linearized state and input matrices

$$\check{\mathbf{x}}_{k+1} = \mathbf{f}(\hat{\mathbf{x}}_k, \mathbf{u}_k) \tag{22}$$

$$\check{\mathbf{P}}_{k+1} = \mathbf{F}_k \hat{\mathbf{P}}_k \mathbf{F}_k^\top + \mathbf{G}_k \mathbf{Q} \mathbf{G}_k^\top \tag{23}$$

2) *Correction*: In the correction step, the state estimation and error covariance estimate is updated using exteroceptive measurements, the measurement model (21) and the linearized measurement matrix

$$\tilde{\mathbf{y}}_k = \mathbf{z}_k - \mathbf{h}(\mathbf{x}_k) \tag{24}$$

$$\mathbf{K}_k = \check{\mathbf{P}}_k \mathbf{H}_k^\top \mathbf{W}_k^{-1} \quad \text{where } \mathbf{W}_k = \mathbf{H}_k \check{\mathbf{P}}_k \mathbf{H}_k^\top + \mathbf{R} \tag{25}$$

$$\hat{\mathbf{x}}_{k+1} = \check{\mathbf{x}}_k + \mathbf{K}_k \tilde{\mathbf{y}}_k \tag{26}$$

$$\hat{\mathbf{P}}_{k+1} = \check{\mathbf{P}}_k + \mathbf{K}_k \mathbf{H}_k \check{\mathbf{P}}_k + \check{\mathbf{P}}_k \mathbf{H}_k^\top \mathbf{K}_k^\top + \mathbf{K}_k \mathbf{W}_k \mathbf{K}_k^\top \tag{27}$$

Implementation-wise, the correction equations (24) through (27) are run asynchronously, as soon as measurements from any source out of the three listed previously are received. This ensures that the slowest sensor, i.e. payload relative position which must be measured by some visual fiducial system, does not hold back faster sensors.

VI. Experimental Results

Departing from the past practice for validating our controller's theoretical predecessors [10, 11], our estimation and control framework is first verified in the Gazebo simulation environment [27] before real-life flight tests.

A. Simulated SLTS Path Following Missions

A custom model for an SLTS, comprising a quadrotor (1.52 kg) with a downward facing camera, a payload (0.5kg) tagged by an Apriltag (36h11) [28], and a cable (1.6m), is defined as seen in figure 3a. Two path profiles were defined for our simulation tests. Firstly, a *square* path profile consisting of four 80m long sides at a constant altitude of 10m, to be flown at a speed of 2m/s, was defined

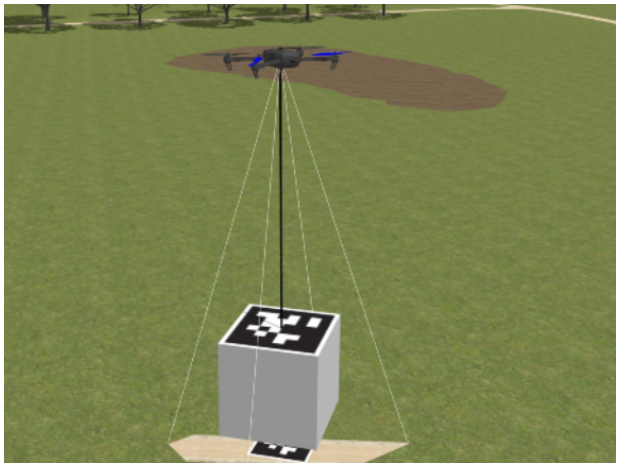

(a) Simulated SLTS Model

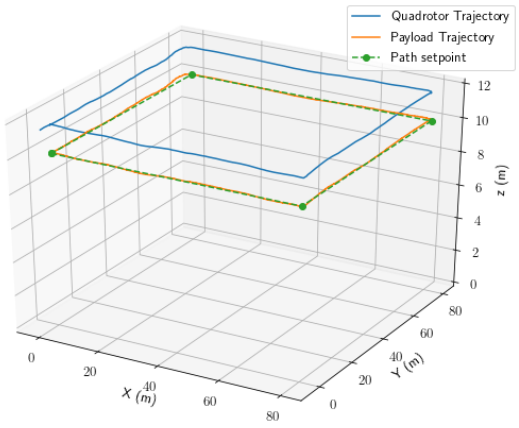

(b) SLTS following a square path

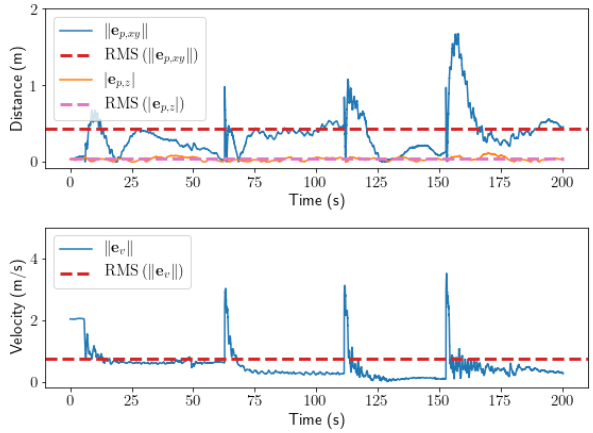

(c) (blue) Payload lateral and (orange) vertical position error (upper) and velocity error (lower)

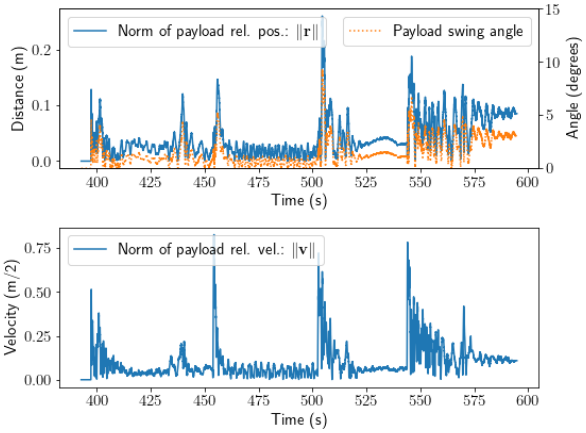

(d) (blue) Payload relative position r and (orange) swing angle (upper) and velocity v (lower)

Fig. 3 Results of square-path following experiment

Figure 3b showed that the SLTS tracked the square path with little visible deviation. Figure 3c quantified this, showing that magnitude of the *lateral* position error is generally less than 0.5410m during level flight, peaking at 1.676m as the SLTS rounds a corner. The root-mean-square (RMS) value of the lateral position error is 0.4381m. *Vertical* position error never exceeded 0.1157m, and its RMS value is merely 0.04343m. The velocity error magnitude is generally less than 0.9817m/s but peaks at 3.512m/s in a turn. Its RMS value is 0.7492m. Figure 3d shows that our controller effectively reduced cable oscillation to almost imperceptible levels during level flight. The magnitude of the payload lateral position relative to the quadrotor is generally less than 0.1380m, spiking up to 0.2609m in a turn. The magnitude of the payload relative velocity is below 0.4188 m/s in level flight while peaking at 0.8264m/s in turns.

Secondly, a near-circular mission profile consisting of a circle 15 meters in radius at a constant altitude of 10m, split into 10 straight segments, to be flown at a speed of 2m/s is defined.

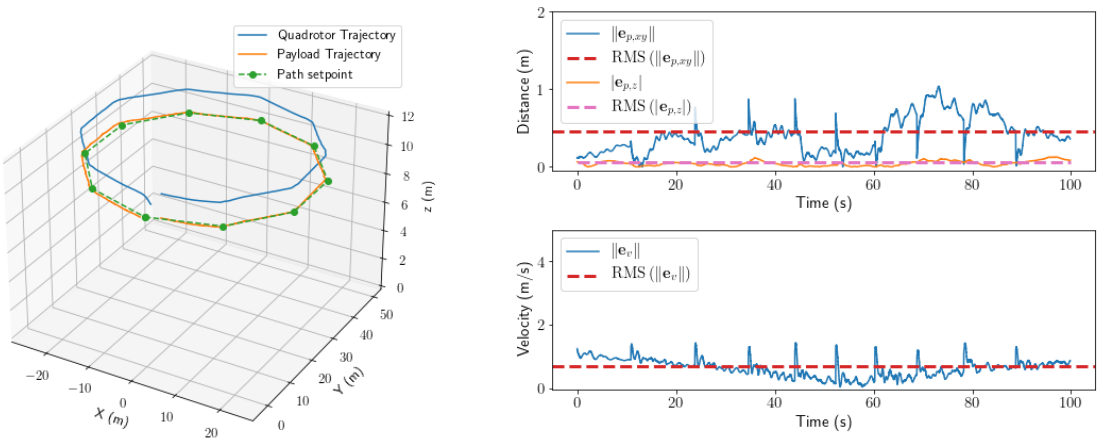

(a) SLTS following a near-circle path

(b) (blue) Payload lateral and (orange) vertical position error (upper) and velocity error (lower)

Fig. 4 Results of circle path following experiment

Figure 4a showed that the SLTS tracked the near-circle path with some slightly visible deviations. This is quantified by Figure 4b which shows that the magnitude of the *lateral* position error is less than 1.040m at all times and its RMS value is 0.4619m. *Vertical* position error never exceeded 0.1182m, and its RMS value is 0.5515m. The magnitude of velocity error never exceeds 1.4306m/s, and its RMS value is 0.6912m.

In summary, the SLTS exhibited acceptable position-tracking errors in simulation exercises. Although the SLTS did not meet the same high level of tracking accuracy, demonstrated in the first experiment, during the circle path following experiment, this is expected because controller gains were tuned to favor payload swing suppression over aggressive position tracking, such that the payload is less likely to swing out of the camera's field of view.

B. State Estimator Evaluation

The performance of the GP-EKF is quantitatively evaluated on payload relative position estimation performance.

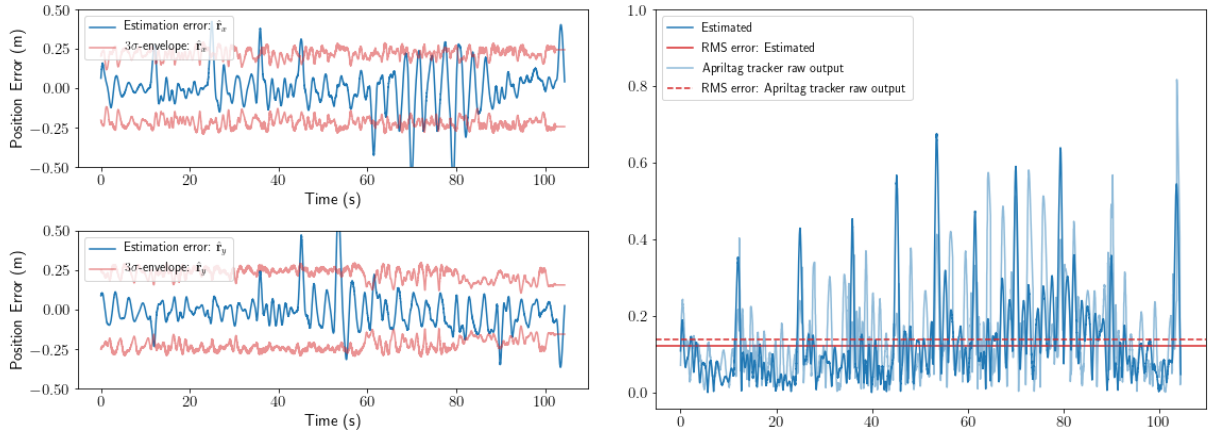

(a) Estimation Error in payload relative position (r) along the x (upper) and y (lower) axis

(b) Magnitude of error in payload relative position, with and without GP-EKF

Fig. 5 Performance of GP-EKF in estimating payload relative position

Figure 5a shows the payload relative position error from the GP-EKF about each axis, each with a 3σ envelope showing the estimated standard deviation of payload relative position estimation. The 3σ envelope bracketed the estimation error in most places, showing that the standard deviation estimation is consistent.

Figure 5b shows the magnitude of the payload relative position error from the GP-EKF (solid-blue line) and the visual fiducial system (semi-transparent blue line). This error is the Euclidean Norm of the difference between the estimated $\mathbf{r}$ and the ground truth value. The maximum payload relative position error estimated by the GP-EKF is 0.6766m whereas that measured by Apriltag tracking is 0.8177m. The RMS value of these errors is 0.1377 and 0.1234 respectively. As expected, including the GP-EKF leads to greater accuracy in payload relative position estimation $\mathbf{r}$. An additional observation is that the GP-EKF outperforms raw Apriltag tracking with more payload swing.

C. Outdoor Flight Tests of SLTS Path Following Missions

For outdoor flight tests, a custom quadrotor (shown in flight in Figure 6a) is used. This quadrotor vehicle weighs 1.09kg and has a thrust-to-weight ratio of approximately 3:1. The payload weighs 0.54kg. A Pixhawk 4 autopilot is used. For absolute position feedback, an UBlox M8N GPS unit is used. For payload position feedback, a downward-facing Raspberry Pi camera is used for observing the payload. Our controller runs on a Jetson Nano onboard computer, which is connected to the autopilot by a serial data link and communicates with a ground control station via a WiFi link, whose effective range is 50m with outdoor WiFi extenders.

For flight tests, a square path profile comprising four 10m sides at an altitude of 10m, to be flown at 2m/s, is defined.

(a) SLTS airborne in flight tests

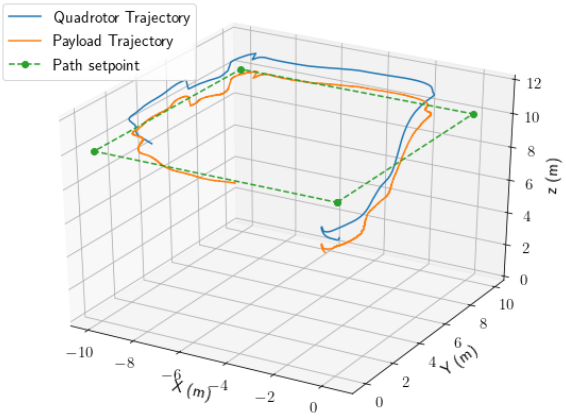

(b) SLTS following a square path

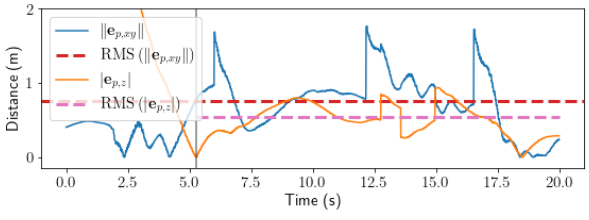

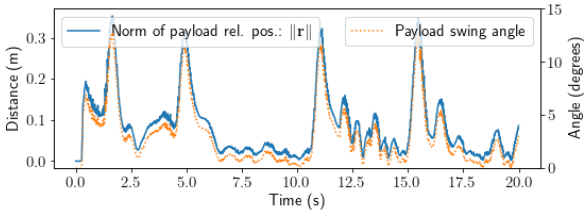

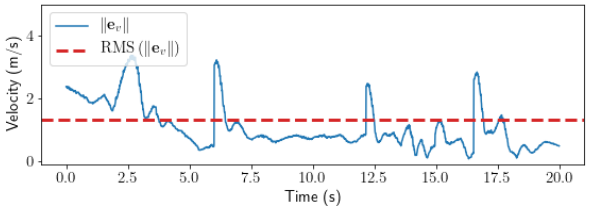

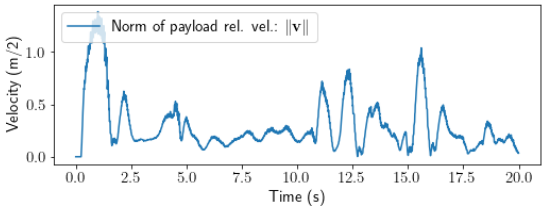

(c) Payload lateral (blue) and vertical (orange) position error (upper) and velocity error (lower)

(d) (blue) Payload relative position r and (orange) swing angle (upper) and velocity v (lower)

Fig. 6 Results of outdoor flight tests

Figure 6b shows that the SLTS tracked the square path successfully, with visible vertical deviation during $0.0s < t \leq 5.26s$ when the SLTS is actively ascending to the set height. Otherwise, Figure 6c shows that the magnitude of *lateral* position error is largely below 1.0m, with spikes up to 1.766m during turning. The RMS value of this *lateral* position error is 0.7519m. On the vertical axis, the SLTS ascended 2.952m over $0.0s < t \leq 5.26s$. Then, it tracked the desired altitude with a vertical position error of no more than 0.9413m. The RMS value of the vertical position error is 0.5468m. Furthermore, the magnitude of velocity error is no more than 1.257m during level flight (i.e. only considering $t > 5.0s$), only spiking up to 3.3718m/s during turning. The RMS value of velocity error magnitude is 1.321m.

The SLTS path tracking accuracy in outdoor flight tests is comparable with that shown in simulations, with the circle path following simulation (Figure 4) bridging the gap between the idealized results from the square path following simulation (Figure 3) and the results of outdoor flight tests here. Furthermore, *robustness to actuator model uncertainty* was demonstrated by our controller, since actuators output less thrust than what was modeled for during flight tests, likely due to battery voltage sag. Our controller was able to compensate for the initial shortfall in thrust force and bring the SLTS to the desired altitude within 5.26 seconds.

Figure 6d shows that our controller reduces payload oscillation to acceptable levels as well. The magnitude of the payload lateral position relative to the quadrotor is no more than 0.1598m generally while spiking to 0.3532 as the SLTS rounds a corner. This corresponds to a 12.5-degree swing angle at worst. Similarly, despite fluctuations in the magnitude of payload relative velocity, including peaks as the SLTS turns, the value of payload relative velocity never exceeds 1.384m/s. This reflected a similar level of performance in limiting payload motion compared to results from simulations.

VII. Conclusion

In this work, a novel GP-EKF and Robust Path-Following Controller framework for a Quadrotor Slung Load Transport System is proposed. A robust controller that is based on a predecessor with proven stability qualities was developed. To provide feedback for this controller, an Extended Kalman Filter, using Gaussian-Process augmented SLTS dynamics as its process model is proposed.

Simulations of path-following missions, followed by flight tests in outdoor conditions, were carried out to demonstrate the capability of our framework. The SLTS was stabilized on the reference path with an accuracy on the order of a few meters, and payload motion relative to the transporting SLTS during the mission was effectively suppressed. These claims are verified in outdoor conditions, where wind disturbances and model uncertainty take a visible toll, but are effectively overcome by our estimation and control framework. Furthermore, our own previous works, albeit the basis for our robust controller, were verified exclusively in indoor environments aided by motion capture systems. With these flight tests, our previous work is surpassed.

In the future, more work can be done to qualitatively evaluate the impact on path-following performance by each element, i.e. the EKF, the GP, and the robust controller, in our framework. Moreover, a fine-grained formulation of GPs may be proposed to correct a specific aspect of SLTS model inaccuracy, such as the effects of cable flexibility.

To aid future work, our implementation of the core robust controller is open-sourced at `https://github.com/Hs293Go/slts_control`

Funding Sources

This research is sponsored by the Natural Science and Engineering Council of Canada (NSERC) Collaborative Research Program in collaboration with Drone Delivery Canada (Funding No CRDPJ 508381-16),

References

[1] Palunko, I., Cruz, P., and Fierro, R., "Agile load transportation: Safe and efficient load manipulation with aerial robots," *IEEE robotics & automation magazine*, Vol. 19, No. 3, 2012, pp. 69–79.

[2] Sreenath, K., Lee, T., and Kumar, V., "Geometric control and differential flatness of a quadrotor UAV with a cable-suspended load," *52nd IEEE Conference on Decision and Control*, IEEE, 2013, pp. 2269–2274.

[3] Dai, S., Lee, T., and Bernstein, D. S., "Adaptive control of a quadrotor UAV transporting a cable-suspended load with unknown mass," *53rd IEEE Conference on Decision and Control*, IEEE, 2014, pp. 6149–6154.

[4] Guerrero, M. E., Mercado, D., Lozano, R., and García, C., "Passivity based control for a quadrotor UAV transporting a cable-suspended payload with minimum swing," *2015 54th IEEE Conference on Decision and Control (CDC)*, IEEE, 2015, pp. 6718–6723.

[5] Sreenath, K., Michael, N., and Kumar, V., "Trajectory generation and control of a quadrotor with a cable-suspended load-a differentially-flat hybrid system," *2013 IEEE international conference on robotics and automation*, IEEE, 2013, pp. 4888–4895.

[6] Zürn, M., Morton, K., Heckmann, A., McFadyen, A., Notter, S., and Gonzalez, F., "MPC controlled multirotor with suspended slung load: System architecture and visual load detection," *2016 IEEE Aerospace conference*, IEEE, 2016, pp. 1–11.

[7] Li, G., Tunchez, A., and Loianno, G., "Pcmpc: Perception-constrained model predictive control for quadrotors with suspended loads using a single camera and imu," *2021 IEEE International Conference on Robotics and Automation (ICRA)*, IEEE, 2021, pp. 2012–2018.

[8] Qian, L., and Liu, H. H., "Dynamics and control of a quadrotor with a cable suspended payload," *2017 IEEE 30th Canadian Conference on Electrical and Computer Engineering (CCECE)*, IEEE, 2017, pp. 1–4.

[9] Qian, L., and Liu, H. H., "Path-following control of a quadrotor UAV with a cable-suspended payload under wind disturbances," *IEEE Transactions on Industrial Electronics*, Vol. 67, No. 3, 2019, pp. 2021–2029.

[10] Qian, L., and Liu, H. H., "Path Following Control of Multiple Quadrotors Carrying A Rigid-body Slung Payload," *AIAA Scitech 2019 Forum*, 2019, p. 1172.

[11] Qian, L., and Liu, H. H., "Robust Control Study for Tethered Payload Transportation Using Multiple Quadrotors," *Journal of Guidance, Control, and Dynamics*, Vol. 45, No. 3, 2022, pp. 434–452.

[12] Tang, S., Wüest, V., and Kumar, V., "Aggressive flight with suspended payloads using vision-based control," *IEEE Robotics and Automation Letters*, Vol. 3, No. 2, 2018, pp. 1152–1159.

[13] Aghdam, A. S., Menhaj, M. B., Barazandeh, F., and Abdollahi, F., "Cooperative load transport with movable load center of mass using multiple quadrotor UAVs," *2016 4th International Conference on Control, Instrumentation, and Automation (ICCIA)*, IEEE, 2016, pp. 23–27.

[14] Lee, H.-I., Yoo, D.-W., Lee, B.-Y., Moon, G.-H., Lee, D.-Y., Tahk, M.-J., and Shin, H.-S., "Parameter-robust linear quadratic Gaussian technique for multi-agent slung load transportation," *Aerospace Science and Technology*, Vol. 71, 2017, pp. 119–127.

[15] Geng, J., and Langelaan, J. W., "Estimation of inertial properties for a multilift slung load," *Journal of Guidance, Control, and Dynamics*, Vol. 44, No. 2, 2021, pp. 220–237.

[16] Goodarzi, F. A., and Lee, T., "Dynamics and control of quadrotor UAVs transporting a rigid body connected via flexible cables," *2015 american control conference (ACC)*, IEEE, 2015, pp. 4677–4682.

[17] Goodarzi, F. A., Lee, D., and Lee, T., "Geometric stabilization of a quadrotor UAV with a payload connected by flexible cable," *2014 American Control Conference*, IEEE, 2014, pp. 4925–4930.

[18] Goodarzi, F. A., Lee, D., and Lee, T., "Geometric control of a quadrotor UAV transporting a payload connected via flexible cable," *International Journal of Control, Automation and Systems*, Vol. 13, No. 6, 2015, pp. 1486–1498.

[19] Kotaru, P., Wu, G., and Sreenath, K., "Dynamics and control of a quadrotor with a payload suspended through an elastic cable," *2017 american control conference (ACC)*, IEEE, 2017, pp. 3906–3913.

[20] Kang, K., Prasad, J., and Johnson, E., "Active control of a uav helicopter with a slung load for precision airborne cargo delivery," *Unmanned Systems*, Vol. 4, No. 03, 2016, pp. 213–226.

[21] Vargas Moreno, A. E., "Machine learning techniques to estimate the dynamics of a slung load multirotor UAV system," Ph.D. thesis, University of Glasgow, 2017.

[22] Ko, J., Klein, D. J., Fox, D., and Haehnel, D., "GP-UKF: Unscented Kalman filters with Gaussian process prediction and observation models," *2007 IEEE/RSJ International Conference on Intelligent Robots and Systems*, IEEE, 2007, pp. 1901–1907.

[23] Ko, J., and Fox, D., "GP-BayesFilters: Bayesian filtering using Gaussian process prediction and observation models," *Autonomous Robots*, Vol. 27, No. 1, 2009, pp. 75–90.

[24] Williams, C. K., and Rasmussen, C. E., *Gaussian processes for machine learning*, Vol. 2, MIT press Cambridge, MA, 2006.

[25] Roza, A., and Maggiore, M., "A class of position controllers for underactuated VTOL vehicles," *IEEE Transactions on Automatic Control*, Vol. 59, No. 9, 2014, pp. 2580–2585.

[26] Solak, E., Murray-Smith, R., Leithead, W., Leith, D., and Rasmussen, C., "Derivative observations in Gaussian process models of dynamic systems," *Advances in neural information processing systems*, Vol. 15, 2002.

[27] Koenig, N., and Howard, A., "Design and use paradigms for gazebo, an open-source multi-robot simulator," *2004 IEEE/RSJ International Conference on Intelligent Robots and Systems (IROS)(IEEE Cat. No. 04CH37566)*, Vol. 3, IEEE, 2004, pp. 2149–2154.

[28] Wang, J., and Olson, E., "AprilTag 2: Efficient and robust fiducial detection," *2016 IEEE/RSJ International Conference on Intelligent Robots and Systems (IROS)*, IEEE, 2016, pp. 4193–4198. https://doi.org/10.1109/IROS.2016.7759617.